Influence of solar wind–magnetosphere coupling functions on the *Dst* index

E. Spencer,[1] P. Kasturi,[1] S. Patra,[1] W. Horton,[2] and M. L. Mays[3]

Received 25 April 2011; revised 21 September 2011; accepted 17 October 2011; published 30 December 2011.

[1] In this paper we investigate the role of different solar wind magnetosphere coupling functions on the *Dst* index calculated by the low-order nonlinear dynamical WINDMI model. In our previous work we have shown that the geotail current dynamics has a significant role in the two-phase decay of the *Dst* index. During that investigation we used the rectified solar wind electric field v_xB_z as a baseline for the simulations and analysis. Here we include an evaluation of four other coupling functions in addition to the rectified vB_s. These coupling functions emphasize different physical mechanisms to explain the energy transfer into the magnetosphere due to solar wind velocity, dynamic pressure, magnetic field, and Mach number. One coupling function is due to Siscoe, another by Borovsky, and two by Newell. Our results indicate that for a majority of cases, at most only v_x, B_y, and B_z are needed to sufficiently account for the supply of energy to the ring current and geotail current components that contribute to the *Dst* index. The more complex coupling functions sometimes perform extremely well on storm data sets but at other times do not reproduce the *Dst* index faithfully. The *AL* index was used as an additional constraint on the allowable geotail current dynamics and to further differentiate between coupling functions when the *Dst* performance was similar. The solar wind dynamic pressure contribution appears to be correctly accounted for through the calculation of the *Dmp* formula of Burton et al. (1975). The degree to which the B_y component affects the *Dst* index is not entirely clear from our results, but in most cases its inclusion slightly overemphasizes the ring current contribution and slightly underemphasizes the geotail current contribution.

Citation: Spencer, E., P. Kasturi, S. Patra, W. Horton, and M. L. Mays (2011), Influence of solar wind–magnetosphere coupling functions on the *Dst* index, *J. Geophys. Res.*, *116*, A12235, doi:10.1029/2011JA016780.

1. Introduction

[2] The *Dst* index is an indicator of the change in magnetic field observed on the surface of the Earth due to changes in the magnetospheric current systems. The ring current and the cross-tail current produce southward or negative perturbations to the dipole magnetic field measured on the surface of the Earth. In addition to this, compression of the dayside magnetosphere from solar wind dynamic pressure contributes to positive perturbations of the *Dst* index. The largest changes in the *Dst* occur during the geomagnetic storms triggered by coronal mass ejections (CMEs) and corotating interaction regions (CIRs) originating from the Sun.

[3] How much of the measured *Dst* is due to each of the different current systems remains to be understood. It has been reported previously [*Alexeev et al.*, 1996; *Feldstein and Dremukhina*, 2000; *Alexeev et al.*, 2001; *Maltsev et al.*, 1996; *Tsyganenko and Sitnov*, 2005] that the tail current is a major contributor to the *Dst* index during storm time, although the relative contribution is still debated [*Turner et al.*, 2000; *Maltsev and Ostapenko*, 2002]. The *Dst* decay during a geomagnetic storm is observed to follow a two-phase pattern, a period of fast decay followed by a phase where the *Dst* returns to its quiet time value gradually [*Takahashi et al.*, 1990; *Feldstein and Dremukhina*, 2000; *Kozyra et al.*, 1998]. The role of different current systems and decay mechanisms in explaining this observation is still under investigation.

[4] *Alexeev et al.* [1996] and *Maltsev et al.* [1996] report equal or even higher tail current contribution to *Dst*. According to *Turner et al.* [2000] and *Baker et al.* [2001], there is only a 25% contribution of magnetotail current (DT) to *Dst* during magnetic storms. On the other hand, *Maltsev and Ostapenko* [2002] suggest about 80% contribution of Dt, although using a slightly different definition of the tail current that that of *Turner et al.* [2000]. *Liemohn et al.* [2001] and *Kozyra et al.* [2002] reported a strong agreement between modeled *Dst* due to ring current and observed *Dst* fields, which implies a minimal (even no) contribution of DT to *Dst* at the maximum of the storm main phase.

[1]Center for Space Engineering, Utah State University, Logan, Utah, USA.
[2]Space and Geophysics Laboratory, University of Texas at Austin, Austin, Texas, USA.
[3]NASA Goddard Space Flight Center, Greenbelt, Maryland, USA.

Tsyganenko and Sitnov [2005] found that the symmetric and the tail current are the most significant contributors to the *Dst* index. According to them, in most cases the tail field even exceeds that of the ring current during the main phase, but then quickly subsides, leaving the symmetrical ring current as the dominant source through the rest of the recovery phase.

[5] Using the low-order physics based WINDMI model, we showed [*Patra et al.*, 2011] that the two phase decay could be explained by including the magnetic field due to the geotail current. The geotail current contributed significantly to the initial fast decay while the ring current provided the slower decay in the *Dst* signal. We also found that by including the magnetic contributions from the magnetopause currents through the calculation of the *Dmp* [*Burton et al.*, 1975], the resultant total calculated *Dst* from the WINDMI model showed a remarkably high fidelity to the actual measured *Dst* for thirteen 3–10 day long geomagnetic storm events that occurred between 2000 and 2007.

[6] The solar wind velocity, interplanetary magnetic field and proton density all play a role in transferring energy into the magnetosphere. However, an exact coupling function quantitatively describing the contribution from the solar wind parameters is as yet undecided. The y-directed component of the solar wind rectified electric field E_y as seen in the Earth's reference frame given by $\mathbf{v} \times \mathbf{B}$ is commonly used as a coupling function, called the rectified vB_s coupling function, but there are many others. *Newell et al.* [2007] derived a coupling function and compared its performance against many other functions, while *Siscoe et al.* [2002a], *Borovsky* [2008], *Lyatsky et al.* [2007], and *Balikhin et al.* [2010] have produced other coupling functions.

[7] The performance of these coupling functions has often been compared with regard to their correlation to the *Dst* index. *Spencer et al.* [2009] compared the performance of the rectified Siscoe and Newell coupling functions in reproducing and predicting the westward auroral electrojet AL index as well as the *Dst* index. There we found that the rectified vB_s performed more robustly in prediction compared to the others, but did not perform as well in re-producing the AL indices when doing post-event analysis.

[8] In this work we perform a post-event analysis of a selection of large geomagnetic storms between 2000 and 2002 to test the capability of different coupling functions in reproducing the *Dst* index faithfully. We also analyze the contributions from different current systems as implied by the qualitative differences between the coupling functions. In order to do this we scale the coupling functions appropriately, and use each of them in turn to drive the WINDMI model. The WINDMI model is tuned computationally with a genetic algorithm for the best fit against the measured *Dst* index. The resulting curves are then analyzed and compared between the different inputs. Because the WINDMI model has been successfully used in the past [*Spencer et al.*, 2007; *Horton et al.*, 2003] to analyze substorm dynamics and the AL index signatures associated with solar wind-forcing, we used the AL index as a secondary constraint so that the coupling functions could be differentiated when the *Dst* indexes were similar.

[9] The coupling functions that are evaluated in this work differ from each other in the solar wind parameters used in their calculation. We chose these coupling functions because they have been reported to correlate well to the *Dst* index. For the rectified vB_s, only the solar wind parameters v_x and B_z are considered geoeffective. For the coupling functions given by Siscoe and Newell, the solar wind dynamic pressure, IMF B_y, IMF B_z and the solar wind velocity v_x are considered geoeffective. The coupling function due to Borovsky is based on the idea that the solar wind dynamic pressure and Mach number largely controls the rate of reconnection at the nose of the magnetopause, and therefore controls the rate of energy transfer into the magnetosphere.

[10] This paper is divided into sections as follows. In section 2 we give a description of the WINDMI model. The formulas for the calculation of the *Dst* index due to different contributors is also given in this section. In section 3 we describe briefly how the model is optimized for different storm data. In section 4 we give a synopsis of the different coupling functions that are evaluated in the remainder of the work. In section 5 we give a short explanation of the storm events chosen and the criteria we required for their inclusion. In section 6 we explain our results and categorize the behavior of the different coupling functions. Finally, we summarize and conclude the work in section 7.

2. Description of the WINDMI Model

[11] The plasma physics based WINDMI model uses a solar wind based voltage, V_{sw}, generated by a particular solar wind-magnetosphere coupling function, to drive eight ordinary differential equations describing the transfer of power through the geomagnetic tail, the ionosphere and the ring current. The WINDMI model is described in some detail by *Spencer et al.* [2007]. The equations of the model are given by

$$L\frac{dI}{dt} = V_{\mathrm{sw}}(t) - V + M\frac{dI_1}{dt} \tag{1}$$

$$C\frac{dV}{dt} = I - I_1 - I_{\mathrm{ps}} - \Sigma V \tag{2}$$

$$\frac{3}{2}\frac{dp}{dt} = \frac{\Sigma V^2}{\Omega_{\mathrm{cps}}} - u_0 p K_{\parallel}^{1/2}\Theta(u) - \frac{pVA_{\mathrm{eff}}}{\Omega_{\mathrm{cps}}B_{\mathrm{tr}}L_y} - \frac{3p}{2\tau_E} \tag{3}$$

$$\frac{dK_{\parallel}}{dt} = I_{ps}V - \frac{K_{\parallel}}{\tau_{\parallel}} \tag{4}$$

$$L_I\frac{dI_1}{dt} = V - V_I + M\frac{dI}{dt} \tag{5}$$

$$C_I\frac{dV_I}{dt} = I_1 - I_2 - \Sigma_I V_I \tag{6}$$

$$L_2\frac{dI_2}{dt} = V_I - \left(R_{\mathrm{prc}} + R_{A2}\right)I_2 \tag{7}$$

$$\frac{dW_{\mathrm{rc}}}{dt} = R_{\mathrm{prc}}I_2^2 + \frac{pVA_{\mathrm{eff}}}{B_{\mathrm{tr}}L_y} - \frac{W_{\mathrm{rc}}}{\tau_{\mathrm{rc}}} \tag{8}$$

The nonlinear equations of the model trace the flow of electromagnetic and mechanical energy through eight pairs of

transfer terms. The remaining terms describe the loss of energy from the magnetosphere-ionosphere system through plasma injection, ionospheric losses and ring current energy losses.

[12] In the differential equations the coefficients are physical parameters of the magnetosphere-ionosphere system. The quantities L, C, Σ, L_1, C_I and Σ_I are the magnetospheric and ionospheric inductances, capacitances, and conductances respectively. A_{eff} is an effective aperture for particle injection into the ring current, that on the dusk side merges with what is known as the Alfvén layer [*Doxas et al.*, 2004]. The Alfvén layer is defined to be the separatrix between two sets of drift trajectories, one comprising open drift paths extending from the magnetospheric tail to the dayside magnetopause and another, nearer set consisting of closed drift paths, encircling the Earth [*Wolf et al.*, 2007]. The resistances in the partial ring current and region 2 current, I_2 are R_{prc} and R_{A2} respectively, and L_2 is the inductance of the region-2 current. The coefficient u_0 in equation (3) is a heat flux limiting parameter. The energy confinement times for the central plasma sheet, parallel kinetic energy and ring current energy are τ_E, τ_k and τ_{rc} respectively. The effective width of the magnetosphere is L_y and the transition region magnetic field is given by B_{tr}. The pressure gradient driven current is given by $I_{ps} = L_x(p/\mu_0)^{1/2}$, where L_x is the effective length of the magnetotail. The output of the model are the AL and *Dst* indices, in addition to the magnetospheric field aligned currents. The effect of delayed density enhancements of the plasma sheet due to solar wind-forcing, which will add a time variation to C in equation (2), is not included in the present model.

[13] The parameters are combined appropriately into a vector P_d where $d = 18$. They can be estimated using semi analytical techniques or they can be considered as variables that need to be optimized within physically allowable ranges to fit the data for a given storm. Some parameters, e.g. Ω_{cps}, L, have been approximated analytically using the Tsyganenko magnetic field model and then allowed to vary over a physically reasonable range of values as explained by *Spencer et al.* [2007].

[14] The current I_1 used in the model is that portion of the field aligned region 1 current that maps to the nightside central plasma sheet and is considered to be part of the substorm current wedge that produces the westward auroral electrojet. The auroral *AL* index now follows as a magnetic field perturbation ΔB_{AL} from the ambient terrestrial field due to the westward electrojet current that flows in the E-layer ($\sim$90 – 120 km) in the nightside ionosphere. We estimate the relation between I_1 and the *AL* index by assuming that the current I_1 is related linearly to the AL index by a constant of proportionality [*Spencer et al.*, 2007].

[15] The portion of the *Dst* index due to plasma energy stored in the ring current W_{rc} is given by the Dessler-Parker-Sckopke (DPS) [*Dessler and Parker*, 1959; *Sckopke*, 1966] relation:

$$Dst_{rc} = \frac{\mu_0 W_{rc}(t)}{2\pi B_E R_E^3} \tag{9}$$

where B_E is the Earth's surface magnetic field along the equator.

[16] The ring current energy (W_{rc}) injection terms in the WINDMI model are the first and second terms on the right hand side of equation (8). The current I_2 is a region 2 current that leaves the ionosphere on the dawn side, closes in the ring current and returns to the ionosphere on the dusk side. This secondary loop of current has a self inductance L_2 and drives a current through the partial ring current resistance R_{prc} as well as the resistance of the region 2 current loop footprint R_{A2}. The Joule heating through the resistance R_{prc} energizes the ring current particles. The particles injected across the effective aperture A_{eff} is another source of ring current energy. The ring current energy in the model is assumed to be lost by particles drifting out of orbit or by charge exchange processes at a rate proportional to τ_{rc}. The various loss processes of the ring current particles can be represented by a time dependent τ_{rc}, but we chose a fixed value for it during a given storm.

[17] The major current systems that are considered to contribute to the total *Dst* in the magnetosphere are (1) the magnetopause currents shielding Earth's dipolar magnetic field; (2) the symmetric ring current; (3) the partial ring current, and (4) the cross-tail current along with the closure currents on the magnetopause. All these currents cause magnetic perturbations on the Earth's surface. We add the magnetopause current and cross tail current contributions in addition to the WINDMI ring current in order to calculate the complete simulated *Dst* index. The quiet time values for each current system is included in the WINDMI model calculations. Following *Patra et al.* [2011] we have lumped together the effects of the region one and two currents, I_1, I_2, and the geotail current and proceed to use αI of the geotail current to represent both. The contributions from the magnetopause and tail current systems are given by:

$$Dst_{mp} = a * \sqrt{P_{dyn}} \tag{10}$$

$$Dst_t = \alpha I(t) \tag{11}$$

where Dst_{mp} is the perturbation due to the magnetopause currents and Dst_t is the magnetic field contribution from the tail current $I(t)$ which is modeled by WINDMI as I. We used the value of $a = 15.5$ as suggested by *Burton et al.* [1975]. For a look at the results obtained by using the value ($a = 7.25$), as estimated by *O'Brien and McPherron* [2000], see *Patra et al.* [2011]. P_{dyn} is the dynamic pressure exerted by the solar wind on the Earth's magnetopause. The simulated *Dst* is then given by

$$Dst_{windmi} = Dst_{rc} + Dst_{mp} + Dst_t. \tag{12}$$

[18] Estimates for the value of α can be inferred from calculations similar to those given by *Kamide and Chian* [2007, pp. 364–365], but we chose to make it an optimization variable here. We optimized the value of α for the event that occurred on days 325–335 in the year 2001. This event was chosen because the different storm phases were distinct. The best fit value was found to be 4.3 per *MA*. This value of α was then kept fixed for all the other events.

3. Optimization of the WINDMI Model

[19] The variable coefficients in the WINDMI model are L, M, C, Σ, Ω_{cps}, u_0, I_c, A_{eff}, B_{tr}, L_y, τ_E, $\tau_{\|}$, L_I, C_I, Σ_I, L_2, R_{prc}, R_{A2}, τ_{rc}, and α. These parameters are constrained to a maximum and a minimum physically realizable and

allowable values and combined to form a 18-dimensional search space $S \subset \mathbb{R}^{18}$ over which optimization is performed.

[20] To optimize the WINDMI model, we use one form of the genetic algorithm [*Coley*, 2003] to search the physical parameter space in order to minimize the error between the model output and the measured geomagnetic indices. The optimization scheme was used to select a parameter set for which the outputs from the WINDMI model most closely matches the AL index and the *Dst* index simultaneously. For this work we are interested in the features of the *Dst* index, so we have chosen a higher bias of 0.8 for *Dst* while the AL index was given a weighting of 0.2 in order to maintain a reasonably good fit. There is a strong direct correlation between solar wind parameters and the AL index during geomagnetic activity over hour timescales, so a coupling function that does well on predicting the *Dst* index but produces a poor AL index can be differentiated from the others.

[21] The performance of the algorithm is evaluated by how well the average relative variance (ARV) and correlation coefficient (COR) compare with the measured indices. The average relative variance gives a good measure of how well the optimized model tracks the geomagnetic activity in a normalized mean square sense, while the correlation coefficient shows how well the model tracks the geomagnetic variations above and below its mean value. The ARV is given by

$$ARV = \frac{\Sigma_i (x_i - y_i)^2}{\Sigma_i (\bar{y} - y_i)^2} \tag{13}$$

where x_i are model values, y_i are the data values and $\bar{y}$ is the mean of the data values. In order that the model output and the measured data are closely matched, ARV should be closer to zero. A model giving $ARV = 1$ is equivalent to using the average of the data for the prediction. If $ARV = 0$ then every $x_i = y_i$. ARV values for the AL index above 0.8 are considered poor for our purposes. ARV below 0.5 is considered very good, and between 0.5 to 0.7 it is evaluated based upon feature recovery. For the *Dst* index, and ARV of 0.25 is considered good. Below $ARV = 0.15$ is considered very good, and evaluation is based on mostly qualitative criteria.

[22] The correlation coefficient COR is calculated against the AL index only as a measure of performance but not used as a cost function in the optimization process. COR is given by

$$COR = \frac{\Sigma_i (x_i - \bar{x})(y_i - \bar{y})}{\sigma_x \sigma_y} \tag{14}$$

COR is better when closer to 1. It indicates anti-correlation if the value is close to -1. σ_x and σ_y are the model and data variances, respectively. Typically if the correlation coefficient is above 0.7 the performance is considered satisfactory for the physics based WINDMI model. Both the ARV and COR values are calculated over the period when the most geomagnetic activity occurs. When these criteria are observed to be acceptable, the optimization process is assumed to have reached convergence.

4. Solar Wind Coupling Functions

[23] The input into the WINDMI model is a voltage that is proportional to a combination of the solar wind parameters measured at L1 by the ACE satellite. These parameters are the solar wind velocity v_x, the IMF B_x, B_y, B_z, and the solar wind proton density n_{sw}, measured in GSM coordinates. The input parameters are time delayed to account for propagation of the solar wind to the nose of the magnetosphere at $10R_E$ as given by *Spencer et al.* [2007].

[24] In order to properly compare the *Dst* produced by each input processed by the WINDMI model, we adopted a procedure to normalize the coupling functions, which we discuss in section 6.1. This ensured that only the qualitative differences contributed to the different *Dst* curves produced by each function. Additionally, the same offset voltage of 40 kV was added to each scaled coupling function to drive the ring current and tail current total contribution to the *Dst* index to nominally 2–5 nT of activity during quiet times. In sections 4.1–4.5 we describe each coupling function in turn, and we make note of some key similarities and differences between them.

4.1. Rectified IMF Driver

[25] The first input function chosen for this study is the standard rectified vB_s formula [*Reiff and Luhmann*, 1986], given by

$$V_y = v_{sw} B_s^{IMF} L_y^{eff} (kV) \tag{15}$$

$$V_{sw}^{Bs} = 40(kV) + V_y \tag{16}$$

where v_{sw} is the x-directed component of the solar wind velocity in GSM coordinates, B_s^{IMF} is the southward IMF component and L_y^{eff} is an effective cross-tail width over which the dynamo voltage is produced. For northward or zero B_s^{IMF}, a base viscous voltage of 40 kV is used to drive the system.

4.2. Siscoe Driver

[26] The second input function is using a model given by *Siscoe et al.* [2002a, 2002b] and *Ober et al.* [2003] for the coupling of the solar wind to the magnetopause using the solar wind dynamic pressure P_{sw} to determine the standoff distance. This model includes the effects of the east–west component of the IMF through the clock angle θ_c. The Siscoe formula is given by

$$V_{sw}^{S}(kV) = 40.0(kV) + \nu_s 57.6 E_{sw}(mV/m) P_{sw}^{-1/6}(nPa) \tag{17}$$

where

$$E_{sw} = v_{sw} B_T \sin^2(\theta_c/2) \tag{18}$$

is the solar wind electric field with respect to the magnetosphere and the dynamic solar wind pressure $P_{sw} = n_{sw} m_p v_{sw}^2$. Here m_p is the mass of a proton. The magnetic field strength B_T is the magnitude of the IMF component perpendicular to the x-direction. The IMF clock angle θ_c is given by $\tan^{-1}(B_y/B_z)$. The solar wind flow velocity v_{sw} is taken to be approximately v_x. This voltage is described by *Siscoe et al.* [2002a] as the potential drop around the magnetopause that results from magnetic reconnection in the absence of saturation mechanisms. ν_s is a scaling factor used to normalize

the varying part of the Siscoe coupling function to a specific reference level.

4.3. Newell Driver

[27] The third input function is based on a recent formula from *Newell et al.* [2007] that accounts for the rate of merging of the IMF field lines at the magnetopause. The Newell formula is given by

$$\frac{d\Phi_{MP}}{dt} = v_{sw}^{4/3} B_T^{2/3} \sin^{8/3}(\theta_c/2) \tag{19}$$

This formula is re-scaled to the mean of (15) and given the same viscous base voltage of 40 kV. We obtain the re-scaled Newell formula as

$$V_{sw}^{N} = 40(kV) + \nu_n \frac{d\Phi_{MP}}{dt} \tag{20}$$

where ν_n is a scaling factor used to normalize the varying part of the Newell coupling function to a specific reference level.

4.4. Newell Driver With Dynamic Pressure

[28] *Newell et al.* [2007] found that a modification of the Newell coupling function, $p^{1/2} d\Phi_{mp}/dt$, yielded better correlation results with the *Dst*. We call this modified coupling function the Newell-P function which is then produced as

$$V_{sw}^{NP} = 40(kV) + \nu_{np} p^{1/2} \frac{d\Phi_{MP}}{dt} \tag{21}$$

where ν_{np} is a scaling factor used to normalize the varying part of the Newell-P coupling function to a specific reference level.

4.5. Borovsky Control Function

[29] We also evaluate the performance of the control function derived by *Borovsky* [2008] which expresses the dayside reconnection rate in terms of upstream solar wind parameters. According to Borovsky, the reconnection rate at the dayside magnetopause is governed by four local plasma parameters: B_m, B_s, ρ_m, and ρ_s. Where B_m is the z-component of the magnetic field strength in the magnetosphere just outside the reconnection site, B_s is the z-component of the magnetic field strength in the magnetosheath just outside the reconnection site, ρ_m is the plasma mass density in the magnetosphere just outside the reconnection site, ρ_s is the plasma mass density in the magnetosheath just outside the reconnection site. The magnetosheath parameters are then cast in terms of the upstream solar wind parameters through the use of the Rankine-Hugoniot relations.

[30] The coupling function for solar wind/magnetospheric coupling is derived as

$$R = 0.4\mu_0^{1/2} \sin(\theta/2) \rho_o v_o^2 \left(1 + 0.5 M_{ms}^{-2}\right) \times (1+\beta_s)^{-1/2} \left[C\rho_o + (1+\beta_s)^{-1/2}\rho_m\right]^{-1/2} \times \left[(1+\beta_s)^{1/2} + 1\right]^{-1/2} \tag{22}$$

where ρ_o is the mass density of the solar wind upstream of the bow shock, v_o is the velocity of the solar wind upstream of the bow shock, C is the compression ratio of the bow shock, β_s is the plasma-β value of the magnetosheath plasma near the nose, and M_{ms} is the magnetosonic Mach number of the solar wind. Equation (22) is supplemented with

$$\beta_s = 3.2 \times 10^{-2} M_A^{1.92} \tag{23}$$

$$C = \left\{ [1/4]^6 + [1/(1 + 1.38\log_e(M_A))]^6 \right\}^{-1/6} \tag{24}$$

$$M_{ms} = v_o \left(\left(B_o^2/\mu_o\rho_o\right) + 5P_o/3\rho_o \right)^{-1/2} \tag{25}$$

$$M_A = v_o (\mu_o \rho_o)^{1/2} / B_o. \tag{26}$$

[31] We normalize the Borovsky function with a scaling parameter ν_b to scale it to a specific reference level. With this scaling modification the Borovsky function becomes proportional to a voltage yielding

$$V_{sw}^{B} = 40(kV) + \nu_b R. \tag{27}$$

[32] In using the Borovsky coupling function, we neglected the thermal pressure P_o in equation (25) following *Borovsky* [2008] and used only the dynamic pressure to calculate V_{sw}^{B}. We did this because we expected that the ratio of thermal pressure to dynamic pressure to be low in the solar wind for the events under consideration.

4.6. Discussion on Coupling Functions

[33] First, while the rectified vB_s includes only the southward component of the IMF B_z, the Newell function has the total IMF perpendicular to the x-direction in GSM, and so effectively has $B_y^{2/3}$ when $B_z = 0$. This explains the contribution of B_y to coupling energy into the magnetosphere from this function. For purely northward IMF the Newell function evaluates to zero. The velocity component in the Newell formula is only the x-directed velocity of the solar wind, which is the same as the rectified vB_s, but it is raised to an exponent of 4/3.

[34] The Siscoe coupling function has the solar wind velocity and IMF B_T raised to the exponent 1, but additionally includes the solar wind dynamic pressure explicitly, $\rho_{sw} v_x^2$, which changes the exponent of the solar wind velocity to effectively 2/3. This modification to the exponent for v_x parallels that of the Newell function which also has some solar wind dynamic pressure built into it via pressure balance with the Earth's dipolar magnetic field. The Newell-P coupling function includes the solar wind dynamic pressure explicitly. We chose to include the Borovsky coupling function because of its good correlation to the *Dst* index reported by *Borovsky* [2008]. This function attributes the solar wind coupling efficiency into the magnetosphere largely to solar wind dynamic pressure and Mach number, which is related to the reconnection rate during southward IMF.

5. Storm Events

[35] A set of thirteen events were selected by *Patra et al.* [2011] where the IMF *Bz* turned northward abruptly after the peak in *Dst* index was observed. Under these conditions it is assumed that the flow out losses will be less dominant

and the recovery would be governed by the contributions from the tail current and ring current. For this study we have chosen six events out of the initial thirteen events reported, based on the particular characteristics of each storm. First, we wanted to rate the performance of each coupling function on the storms where the WINDMI model performed best. Second, on some storm events there was data drop out, especially in the proton density over the main phase of the storm.

[36] The 6 events chosen for this study from the previous group of 13 are (1) Days 158–166, 2000, (2) Days 258–266, 2000, (3) Days 225–235, 2001, (4) Days 325–335, 2001, (5) Days 80–88, 2002, and (6) Days 245–260, 2002. In addition to the 6 out of 13 events from *Patra et al.* [2011], we also selected the October 2000 and April 2002 storm events used previously by *Spencer et al.* [2009], since now the inclusion of the tail current contribution and the Dmp contribution adds to the interpretation of the calculated *Dst*.

[37] The solar wind parameters in GSM coordinates required as input to the WINDMI model are obtained from the ACE satellite orbiting at the L1 point between the sun and the Earth. Missing or unusable data from the satellite measurements was dealt with by retaining the previous data value whenever the data was unusable. Hourly AL and *Dst* index values were obtained from the World Data Center for Geomagnetism, Kyoto website.

6. Results and Discussion

6.1. Normalization Methods

[38] The rectified vB_s produces a voltage when v_xB_z is multiplied by an effective width of the magnetosphere of $10R_E$. The Siscoe coupling function already produces a voltage in it's original form. The Newell function and Borovsky function are not suitable in their original formulation for use with the WINDMI model.

[39] The importance of the normalization is that it determines the overall energy that is transferred to the magnetosphere as predicted by a particular coupling function. During various attempts, we tried normalizing the Siscoe, Newell, and Borovsky functions to the rectified vB_s (which we will from here on refer to as *vBs*), first against the *vBs* mean throughout a year, then against the *vBs* mean during a storm event, then against the *vBs* maximum during a storm event. Using these three methods produced some variation in how well each coupling function performed, but did not drastically alter the results.

[40] The most effective method was found to be by using the Siscoe coupling function as a separate basis for normalization. We normalized the Newell, Newell-P, and Borovsky coupling functions to the mean of the Siscoe function over a storm interval as reference. The *vBs* coupling function was not included. This is because the *vBs* was most different from the other four coupling functions in most of the cases, going to zero whenever the IMF Bz has no southward component. This resulted in large time periods over the data set when *vBs* was zero (with a 40 kV offset), while the other coupling functions were all somewhat similarly active. The normalization scheme used ensured that the final form of the coupling functions were different from each other only qualitatively, or in curve shape only, as far as possible. As much potential bias with regards to total energy content of each coupling function was removed.

[41] The various coupling functions are shown in Figures 1, 3, and 5. In Figures 1, 3, and 5 the first four plots show the solar wind data as measured by ACE. The bottom two plots show the relative differences in the amplitudes of the various coupling functions. The siscoe function is plotted in each of these bottom plots as a reference.

[42] To calculate the different normalization constants, we set ν_s for the Siscoe driver to be 1. Then we evaluate ν_n, ν_{np}, and ν_b, the normalization factors for each of the Newell, Newell-P, and Borovsky functions as

$$\nu_X = \left(V_{sw}^X - 40kV\right)\frac{\overline{V_{sw}^S - 40kV}}{\overline{V_{sw}^X - 40kV}} \tag{28}$$

where X represents the one of the Newell, Newell-P, or Borovsky functions, V_{sw}^S is the Siscoe voltage over a storm interval, while $\overline{V_{sw}^X - 40kV}$ represents the mean of the appropriate function to be normalized over the same interval.

6.2. Overall Results

[43] With the different normalization schemes, the optimized results are summarized in Table 1 and Table 2. A full set of figures for every result is provided with the auxiliary material for this paper.[1]

[44] Each coupling function is evaluated over a storm interval using the *vBs* function as a reference for performance quality. When the results were good, the correlation values for such cases exceed 0.8, so the correlation coefficient does not provide a meaningful measure for comparison between the coupling functions. The ARV values for good fits to the *Dst* index are mostly below 0.2, differences below this value are also difficult to identify quantitatively. For this reason qualitative comparisons are done for the most part. The AL index is used to evaluate whether the geotail current signatures are allowable.

[45] The *vBs* function does well enough on all the events to be a reliable coupling function for analysis or predictive purposes. The only function that does as well as *vBs* overall is the Newell coupling function. However, in some cases, one of the other coupling functions fit the features of the storm event better than either *vBs* or Newell. For this reason, we attempted to further refine the evaluation process to get a better representation of the qualities of each coupling function.

[46] The results can be divided into two categories. In the first category (category I), we have storm events where the coupling functions look qualitatively different from each other, but using any coupling function resulted in a good fit to the measured *Dst* data. The events that fall into this category are marked with a "I" in the last column of Table 1. In these events, the relative contributions from each current system due to the different inputs remained roughly the same through the optimization process. We also observed that for the storms in this category, the reproduced *Dst* curves were very good, having an ARV of less than 0.2 in most instances. These storm events were characterized also by their classical nature in that the onset, main phase and decay

[1] Auxiliary material is available in the HTML. doi:10.1029/2011JA016780.

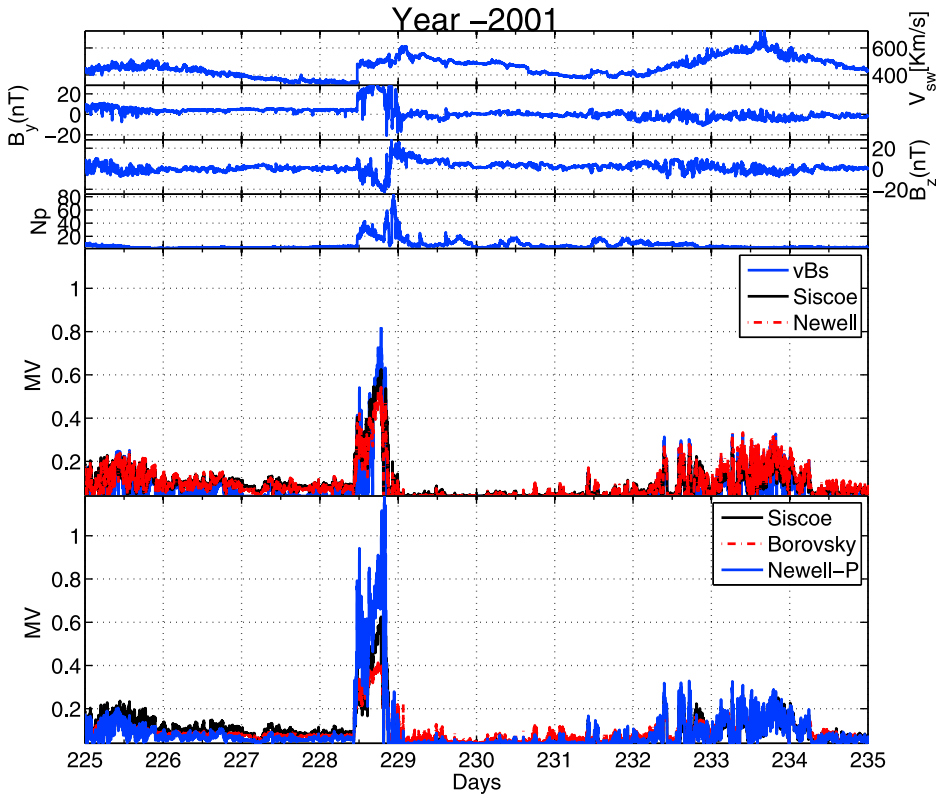

Figure 1. The coupling functions compared for the Category I representative event occurring in year 2001, Days 225–235. The top four plots show the input ACE data. The next plot shows the *vBs* and Newell coupling functions compared to the Siscoe function as reference. The bottom plot shows the Borovsky and Newell-P coupling functions compared to the Siscoe function as reference.

phase are distinct. We discuss one of these events, between days 225–235 in 2001, in section 6.3.

[47] The results in category I do not point to reasonable conclusions about the confidence in each of the coupling functions. In a prediction scheme, using each input with a version of the model that is optimized to that particular function on past training data will result in similar looking *Dst* curves. The best AL index reproduction was obtained mostly by *vBs*. The dynamics of the AL index and therefore the implied geotail current dynamics were acceptable for all storms in this category.

[48] For another category of events, the results were more uncertain. In some cases, the optimization process was able to find different states of the WINDMI model that compensated for the differences between the coupling functions so as to produce a good fit to the measured *Dst* data, but in some cases, either such states did not exist, or the AL index results were not acceptable even though the *Dst* index was reproduced well.

[49] In the case of days 158–166, 2000, for instance, the WINDMI model was not able to produce a good fit to the *Dst* index with the Newell-P function. Further, the AL Index was unusually poor when using this coupling function, giving an ARV of 0.86, compared to *vBs* giving 0.32. In another instance, for the April 15–24 storm event, the Borovsky function produced the best *Dst* index. However, both the Borovsky function and the Newell-P function produced very poor AL indices compared to *vBs* and *Newell*. We classify these cases as falling into category II. We discuss two of these events, days 80–88, 2002, and the April 15–24, 2002 storm, in section 6.4.

[50] The results in category II are difficult to interpret. In this case, if the input coupling functions look different, the output *Dst* curves will be different, and each *Dst* curve may predict different levels of geomagnetic activity over 6–8 hour timescales. In addition, it becomes unclear which version of the optimized model to use for prediction purposes. One possible compromise is to use multiple versions of the model and predict different possible geomagnetic storm scenarios.

[51] The most significant difference in contributions from the ring current and geotail current systems was observed because of the use of *vBs* versus the other three coupling functions. Since *vBs* turns off during periods when there is no southward component of the IMF, the total energy content in *vBs* will be low. In contrast, all the other coupling functions use $B_T = \sqrt{B_z^2 + B_y^2}$, so they do not necessarily turn off during these periods. We found that the overall ring current contribution when using *vBs* was lower than the tail current contribution for these cases. The other coupling functions produce *Dst* curves with a higher ring current contribution compared to the tail current contribution. This is most noticeable in the main phase and decay phase of a storm. The direct interpretation is that the optimized model compensates for lack of total available energy in the coupling function by emphasizing the tail current component when using *vBs*.

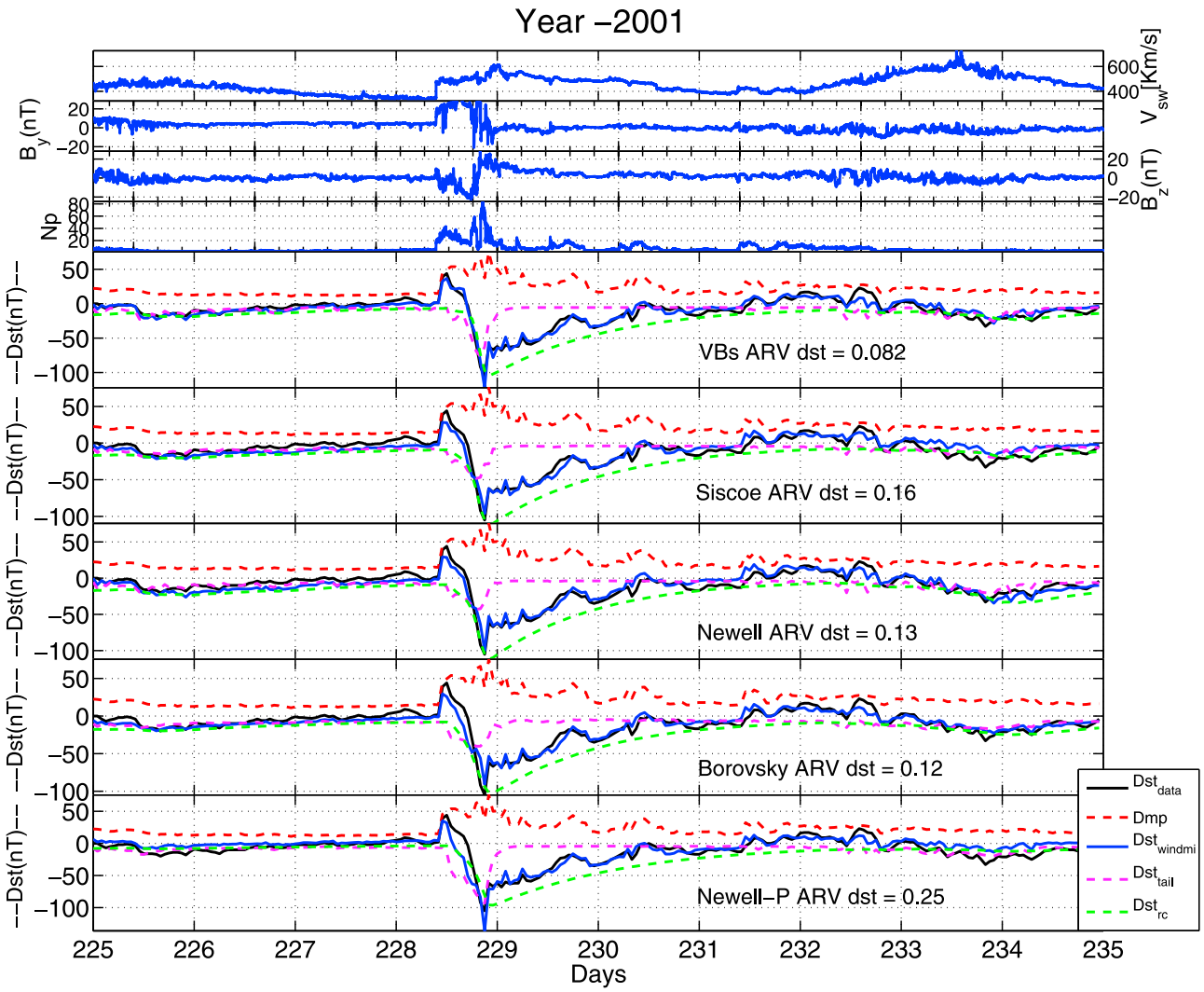

Figure 2. The optimized *Dst* index fits for each coupling function compared for the Category I representative event occurring in year 2001, Days 225–235. The top four plots show the input ACE data. The bottom five plots show the *Dst* fits for each coupling function.

[52] The second difference was the fact that the solar wind dynamic pressure is incorporated into the Siscoe, Borovsky and Newell function (both Newell and Newell-P), but not in *vBs*. Since the solar wind dynamic pressure is also accounted for in the calculation of Dmp, this indicates two possible ways through which the solar wind dynamic pressure contributes. One way is through the depression of the magnetopause, increasing the magnetopause currents and subsequently giving a positive contribution to *Dst* through the Dmp component, and secondly through control of the reconnection rate at the magnetopause, as suggested by *Borovsky* [2008]. This path results in a negative contribution to *Dst* through either the tail current component or the ring current component.

[53] In sections 6.3–6.5 the results in each category are discussed in more detail. For each category we choose some representative events, and proceed to discuss some of its features.

6.3. Category I Events

[54] The representative case for this type of result is the storm event occurring between days 225–235, 2001. To illustrate the differences between the input coupling functions during this event, we show a comparison of the Newell, Newell-P, and Borovsky functions against the *vBs* and Siscoe coupling function for this storm in Figure 1. The Siscoe function is shown in both the top and bottom plots of Figure 1 in order to aid in comparison.

[55] During this event, the initial period between days 226–228 had density data dropout, but this did not affect the results because the density data became available before the sudden storm commencement occurred. The re-produced *Dst* for this event using each of the different coupling functions is shown in Figure 2.

[56] For this storm the sudden storm commencement (SSC), the main phase, and the decay phase, are very well defined. The SSC is captured due to the Dmp contribution, and the ring current and tail current contributions both decay after northward turning occurs as shown by *vBs*, and their relative strengths do not vary significantly from using different coupling functions. The Dmp takes care of most of the short timescale *Dst* dynamics after northward turning. The AL index is fit well (see auxiliary material) with all the

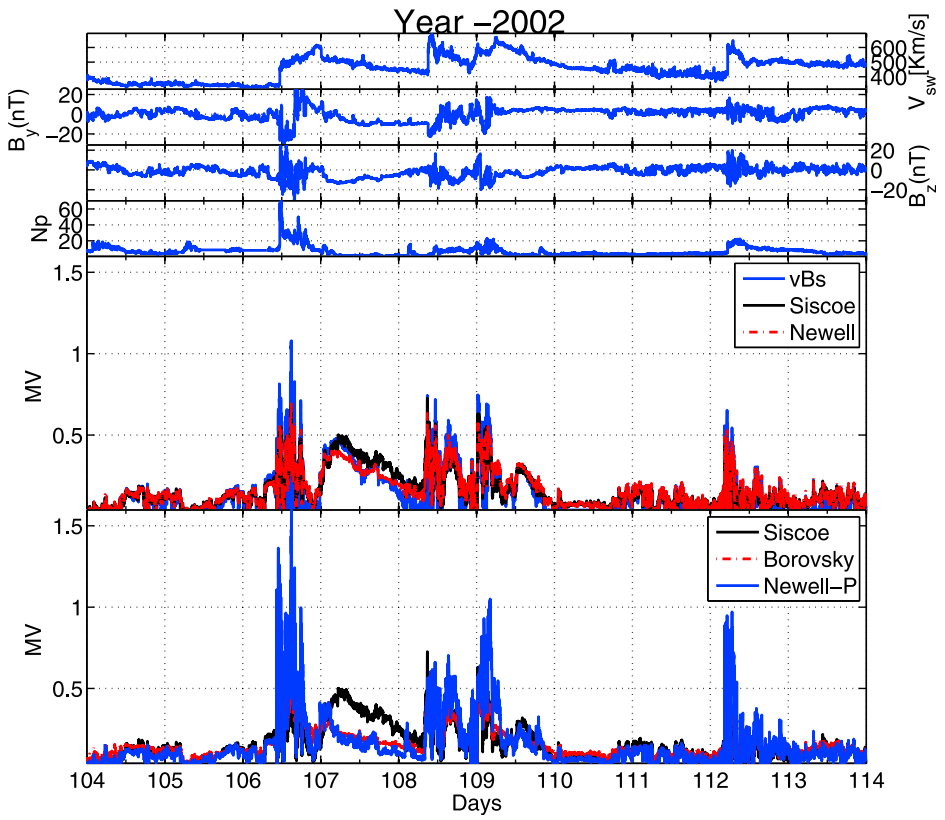

Figure 3. The coupling functions compared for the Category II representative event occurring in year 2002, Days 104–114 (April 15–24, 2002). The top four plots show the input ACE data. The next plot shows the *vBs* and Newell coupling functions compared to the Siscoe function as reference. The bottom plot shows the Borovsky and Newell-P coupling functions compared to the Siscoe function as reference.

coupling functions for this particular event. Similar results were obtained for the rest of the category I events. One exception to this was the results from days 245–260 with the Newell-P coupling function, where the geotail current contribution was larger than the geotail currents produced by the other coupling functions. The AL prediction for the storm on days 325–335, 2001 are affected by the loss of solar wind data during the initial phase of the storm. This is reflected in the ARV numbers of AL for the storm as shown in Table 2.

6.4. Category II Events

[57] In this category, the coupling functions are qualitatively different, and the results also look different. Here we have events on which some coupling functions do well, but others do not. We choose two events that fall into this category, the April 15–24, 2002 storm, and days 80–88, 2002, to illustrate some of the differences in performance.

[58] The first representative event for this category is the April 15–24, 2002 geomagnetic storm. For this event, the input coupling functions are shown in Figure 3. The output *Dst* curves for this event are shown in Figure 4. On this event, the Siscoe coupling function produced the poorest *Dst* index, compared to *vBs* or Newell fits.

[59] There are qualitative differences between the fits to the measured *Dst* produced by *vBs*, Newell and Borovsky coupling functions, but in our estimation they are good fits, with slightly different qualitative features. The slight differences in tail current and ring current contributions differ between each coupling function, which gives rise to the overall difference in the calculated *Dst* between them. Note that the Dmp contribution due to magnetopause currents are exactly the same whatever coupling function is used.

[60] For the Borovsky and Newell-P functions, during the storm main phase, days 107–108, the AL index was very poorly represented. This is an obvious characteristic entirely due to the shape of the two coupling functions, but the physical reasons are unclear. The other coupling functions, including Siscoe, produce good AL indices. From Figure 3, it can be seen that the Siscoe and Newell functions are very close in overall character, but their resulting *Dst* curves are very different. The reason is that the *Dst* curves are a result of time integration of the input coupling functions, so the slight differences that are sustained over 12–24 hours become amplified.

[61] We contrast the results of the April storm with the results obtained for the storm event on days 80–88, 2002. For this event, the input coupling functions are shown in Figure 5. The output *Dst* plots for all the different coupling functions are shown in Figure 6.

[62] For this event, the surprising result was that the Newell-P function produced an output *Dst* as good as that of the *Dst* produced by *vBs*, and in fact slightly better than the Newell coupling function. In this instance the factor $p^{1/2}$ contributes favorably to improve the Newell-P *Dst*

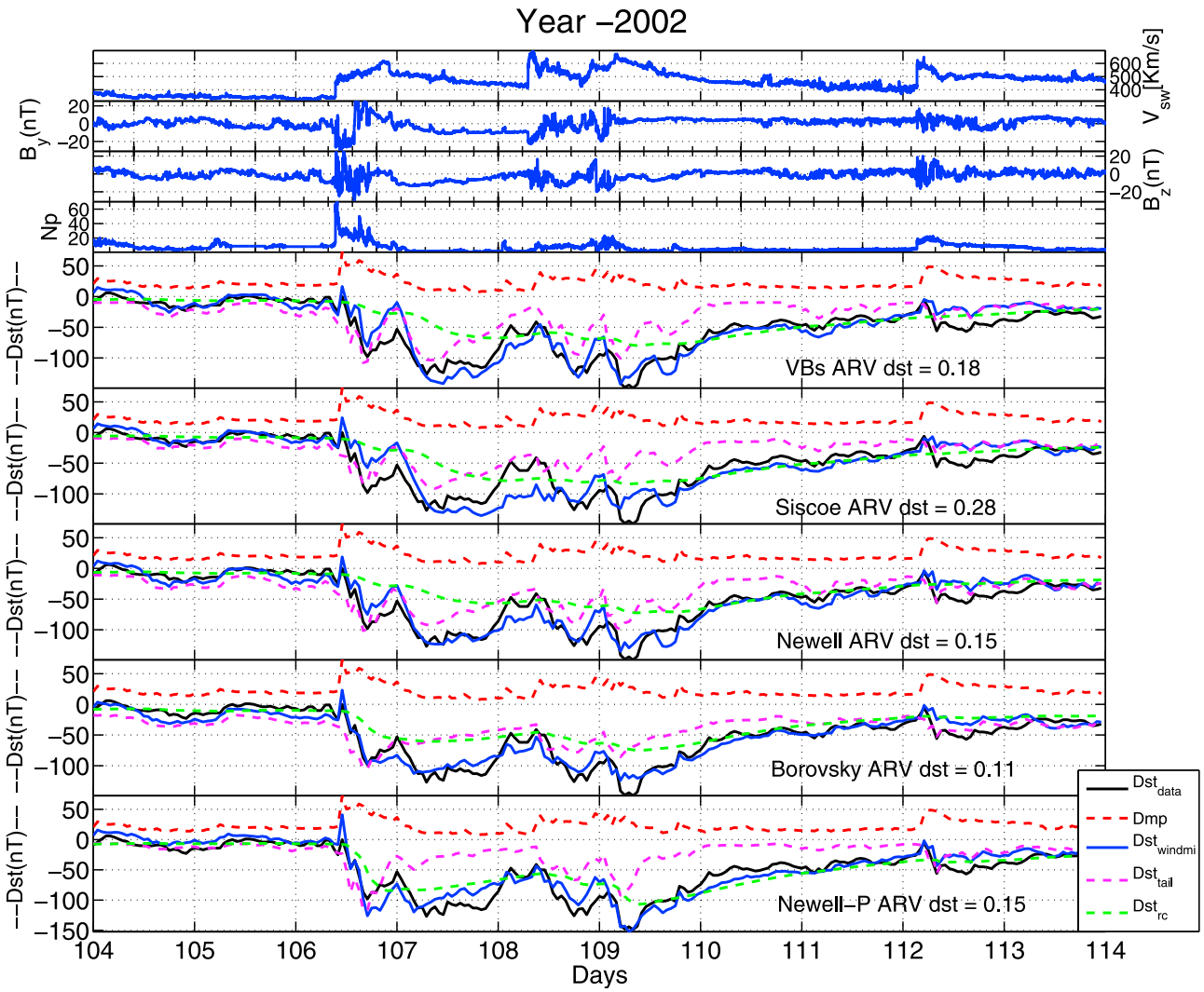

Figure 4. The optimized *Dst* index fits for each coupling function compared for the Category II representative event occurring in year 2002, Days 104–114 (April 15–24, 2002). The top four plots show the input ACE data. The bottom five plots show the *Dst* fits for each coupling function.

calculation. Again, for this storm event, the Siscoe coupling function does not produce a good fit both in *Dst* as well as AL. During this storm, between days 81–82, a density enhancement drives the AL index significantly, because only the Newell-P function amplifies the effect enough to fit the observed AL index.

[63] The Borovsky coupling function, although producing a good fit, is worse than *vBs*, Newell, and Newell-P. All of the four coupling functions that produce good fits have slight differences in the tail to ring current contributions, the Borovsky function producing the highest ring current component. Since the Borovsky, Newell, and Newell-P functions are normalized to the Siscoe coupling function, their energy content is fixed relative to the Siscoe input. The optimization process changes the gain of the WINDMI model in addition to the plasma confinement time constants in order to fit against the data.

[64] Finally, although the Borovsky function produces a good *Dst* index, it does very poorly on the AL index. For this reason we do not accept the Borovsky result with a high degree of confidence for this event. The Borovsky function produced poor AL index curves in all storm data sets except the October 3–7, 2000 storm. The Borovsky function performs well when density enhancements due to shock interfaces are clearly present in the AL and *Dst* signatures.

6.5. Discussion

[65] In both categories of results, the *vBs* and Newell coupling function produce consistently good fits against the data. There are instances where the Borovsky coupling function performs qualitatively as well these two functions, but there are also instances where it does not. Whenever the result is in category I, all functions do well, but for the category II, the Siscoe and Newell-P functions were most inconsistent.

[66] The WINDMI model diverts a portion of the crosstail current into the ionosphere along magnetic field lines (FAC). The AL index therefore becomes proportional to direct solar wind driving unless substorms are triggered. For this reason a coupling function that does not show the ionospheric

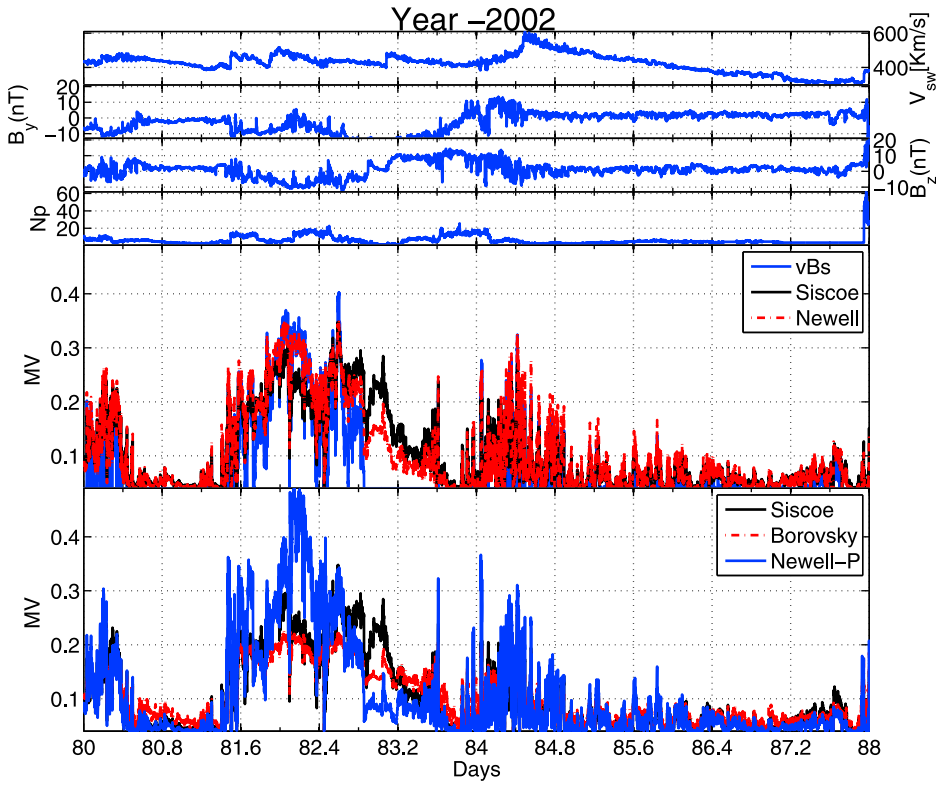

Figure 5. The coupling functions compared for a Category II event that occurred in year 2002, Days 80–88. The top four plots show the input ACE data. The next plot shows the *vBs* and Newell coupling functions compared to the Siscoe function as reference. The bottom plot shows the Borovsky and Newell-P coupling functions compared to the Siscoe function as reference.

current enhancements on hour timescales will not produce a good AL index. The tail current contribution is most closely correlated directly to solar wind activity, with timescale dynamics on the order of 5–20 min, while the ring current represents time integrated energy content that is on the order of 6 hours or more. Thus the fast variations in the *Dst* are a combination of magnetopause Dmp and tail current dynamics, while the slower variations are due to ring current dynamics.

[67] The relative contributions of the tail current to *Dst* for the category I storms is almost similar to the contribution of symmetric ring current to the *Dst* index in the main phase of the storm. The contribution reduces drastically in the recovery phase, as the tail current recovers quickly in the recovery phase leaving the symmetric current as the dominating contributor. The results for category II storms are more variable.

[68] Because the *vBs* function goes to zero during non-southward IMF, the level of energy injection into the ring current is lower with this function over an entire storm than with the Newell function. Because of this, the model produces a larger ring current with the Newell coupling function, and chooses longer decay rates of the ring current during the recovery phase with *vBs*.

[69] Here we note some questions for which the answers are as yet unclear: (1) Why do the *vBs* and Borovsky coupling functions, while appealing to different physics, both produce good results in many cases? (2) Why does the

Table 1. Summary of Results Using Different Coupling Functions With the WINDMI Model Fit Against the Measured *Dst* Index[a]

Year	Storm Event	*vBs*	Siscoe	Newell	Borovsky	Newell-P	Category
2001	225–235	0.082	0.16	0.13	0.12	0.25	I
2001	325–335	0.037	0.033	0.038	0.071	0.042	I
2002	245–260	0.083	0.11	0.1	0.18	0.13	I
2000	158–166	0.16	0.26	0.13	0.17	0.45	II
2000	3–7 Oct	0.088	0.066	0.062	0.13	0.2	II
2000	258–266	0.083	0.17	0.12	0.18	0.16	II
2002	80–88	0.069	0.23	0.09	0.17	0.055	II
2002	15–24 Apr	0.18	0.29	0.15	0.11	0.15	II

[a]In the columns under each input, the ARV values of the calculated *Dst* and the measured *Dst* index for each coupling function are listed. The Category column shows the categorization of the result for the storm event.

Table 2. Summary of Results Using Different Coupling Functions With the WINDMI Model Fit Against the Measured AL Index[a]

Year	Storm Event	*vBs*	Siscoe	Newell	Borovsky	Newell-P	Category
2001	225–235	0.33	0.39	0.34	0.45	0.42	I
2001	325–335	0.57	0.63	0.7	0.74	0.67	I
2002	245–260	0.45	0.43	0.4	0.57	0.57	I
2000	158–166	0.32	0.39	0.32	0.62	0.86	II
2000	258–266	0.64	0.69	0.56	0.78	0.89	II
2000	3–7 Oct	0.3	0.31	0.32	0.4	0.36	II
2002	80–88	0.23	0.51	0.35	0.59	0.25	II
2002	15–24 Apr	0.35	0.37	0.33	0.48	0.59	II

[a]In the columns under each input, the ARV values of the calculated AL and the measured AL index for each coupling function are listed. The Category column shows the categorization of the result for the storm event.

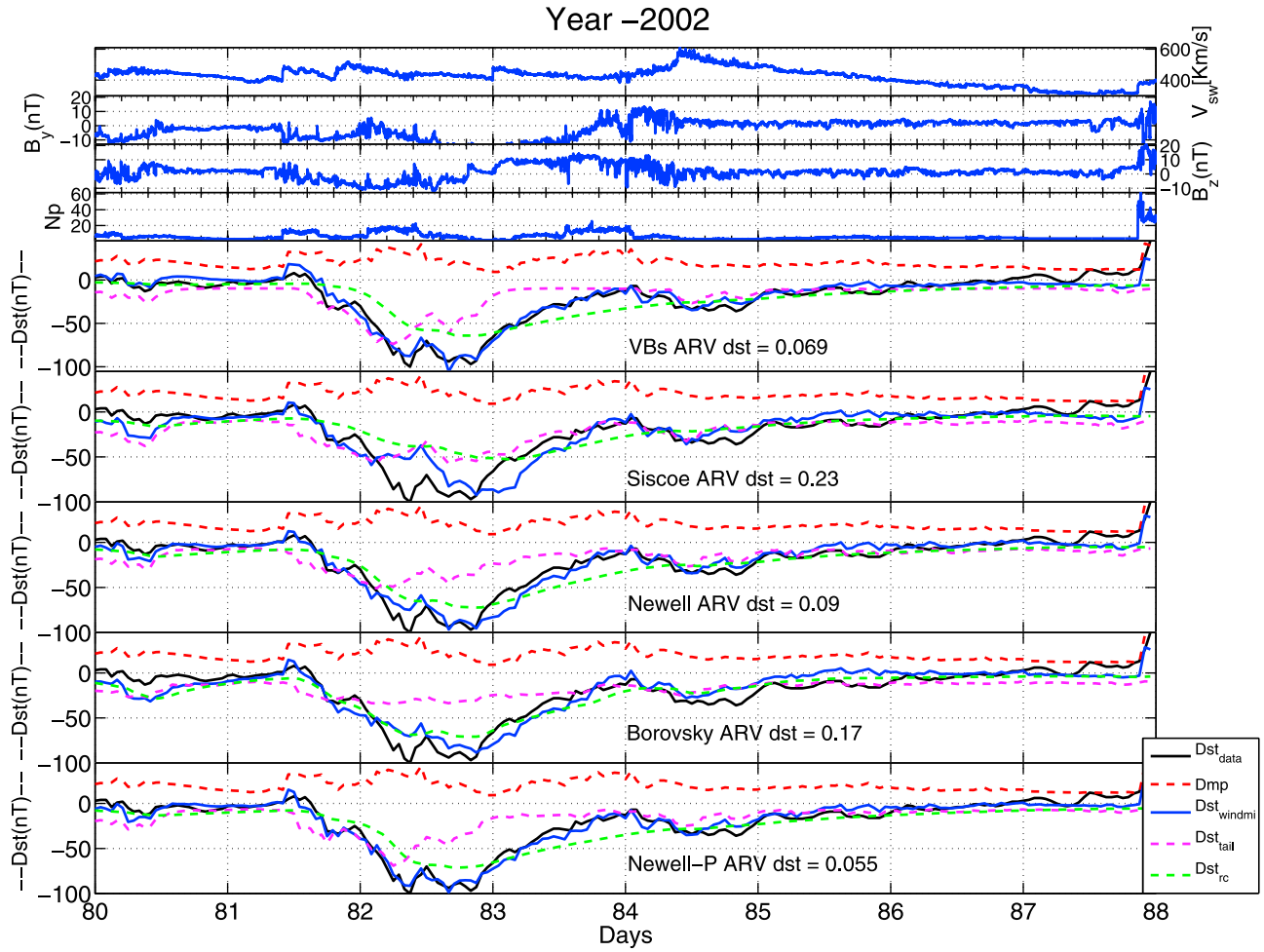

Figure 6. The optimized *Dst* index fits for each coupling function compared for the Category II event that occurred in year 2002, Days 80–88. The top four plots show the input ACE data. The bottom five plots show the *Dst* fits for each coupling function.

inclusion of $p^{1/2}$ to the Newell function produce a bad fit in some cases, but then produce a very good fit in others? (3) Is there a way to get an absolute scale for the energy input instead of using the normalizing procedure used in this work? (4) Is there a conditioning of the magnetosphere from energy injections that explains the differences between category I and category II results? Attempts to answer these questions will motivate our future work.

7. Conclusions

[70] In this work we have examined several different coupling functions and their influence on the *Dst* calculated by the low-order physics based WINDMI model. We chose events from the previous set of 13 given by *Patra et al.* [2011] and two additional large geomagnetic storms that were studied by *Spencer et al.* [2009]. We found that the qualitative character of each coupling function affected the response of the WINDMI model in multiple but categorizable ways. First, the popular rectified vB_s coupling function stands apart in it's qualitative character, because it turns completely off when there is no southward component of the IMF. The other coupling functions were grouped into a second class. These functions variously depended upon IMF B_z as well as B_y, the IMF clock angle, and the solar wind dynamic pressure.

[71] The optimized model results fell into two categories. In the first category, the storm events were such that although the input coupling functions looked qualitatively different from each other, the output results were good fits to the ground measurements of the *Dst* index. In the second category, we had different input coupling functions, but the model was able to compensate for the differences in some instances and still produce good fits to the measured *Dst* indices, while in other cases, it could not. However, if two coupling functions looked very similar, they produced identical results.

[72] Regardless of our classification procedure for the input coupling functions and the categorization of the results, we have been able to draw conclusions as far as the reliability for *Dst* prediction is concerned. In all cases, the rectified *vBs* and the Newell coupling function produced consistently good fits to the measured data. This is evident from Table 1. The extent to which the IMF B_y included in the Newell coupling function exerts an influence on the results cannot be discerned with the WINDMI model unless

there is a way to constrain the level of geotail current contribution from satellite data or perhaps some other technique. In most cases it's inclusion slightly over-emphasizes the ring current contribution, and under-emphasizes the geotail current contribution. Further, since the Newell function contains a component of the solar wind dynamic pressure through pressure balance with the magnetic field across the magnetopause, the separation of effects becomes more difficult.

[73] The Siscoe, Borovsky, and Newell-P coupling functions were most inconsistent in their performance. In some events the results using these coupling functions were not good at all, yet during other events, some of them produced even better fits than either *vBs* or Newell to the measured data. The reason for this is unclear, but the results suggest that either there is an unknown component needed to modulate the coupling functions to produce better results, or that the state of the global magnetosphere varies from event to event in some way that makes one coupling mechanism preferred over the others.

[74] **Acknowledgments.** This work was partially supported under NSF grant NSF-0720201. The solar wind plasma and magnetic field data were obtained from ACE instrument data at the NASA CDA Web site. The geomagnetic indices used were obtained from the World Data Center for Geomagnetism in Kyoto, Japan. W. Horton acknowledges support from the Applied Research Laboratory at the University of Texas and from NSF grant 0964692.

[75] Philippa Browning thanks the reviewers for their assistance in evaluating this paper.

References

Alexeev, I. I., E. S. Belenkaya, V. V. Kalegaev, Y. I. Feldstein, and A. Grafe (1996), Magnetic storms and magnetotail currents, *J. Geophys. Res.*, *101*(A4), 7737–7747.

Alexeev, I. I., V. V. Kalegaev, E. S. Belenkaya, S. Y. Bobrovnikov, Y. I. Feldstein, and L. I. Gromova (2001), Dynamic model of the magnetosphere: Case study for January 9–12, 1997, *J. Geophys. Res.*, *106*(A11), 25,683–25,693.

Baker, D. N., N. E. Turner, and T. I. Pulkkinen (2001), Energy transport and dissipation in the magnetosphere during geomagnetic storms, *J. Atmos. Sol. Terr. Phys.*, *63*, 421–429.

Balikhin, M. A., R. J. Boynton, S. A. Billings, M. Gedalin, N. Ganushkina, D. Coca, and H. Wei (2010), Data based quest for solar wind–magnetosphere coupling function, *Geophys. Res. Lett.*, *37*, L24107, doi:10.1029/2010GL045733.

Borovsky, J. E. (2008), The rudiments of a theory of solar wind/magnetosphere coupling derived from first principles, *J. Geophys. Res.*, *113*, A08228, doi:10.1029/2007JA012646.

Burton, R. K., R. L. McPherron, and C. T. Russell (1975), An empirical relationship between interplanetary conditions and *Dst*, *J. Geophys. Res.*, *80*, 4204–4214.

Coley, D. A. (2003), *An Introduction to Genetic Algorithms for Scientists and Engineers*, World Sci., Tokyo.

Dessler, A., and E. N. Parker (1959), Hydromagnetic theory of geomagnetic storms, *J. Geophys. Res.*, *64*, 2239–2259.

Doxas, I., W. Horton, W. Lin, S. Seibert, and M. Mithaiwala (2004), A dynamical model for the coupled inner magnetosphere and tail, *IEEE Trans. Plasma Sci.*, *32*(4), 1443–1448.

Feldstein, Y. I., and L. A. Dremukhina (2000), On the two-phase decay of the *Dst* variation, *J. Geophys. Res.*, *27*(17), 2813–2816.

Horton, W., R. S. Weigel, D. Vassiliadis, and I. Doxas (2003), Substorm classification with the WINDMI model, *Nonlinear Processes Geophys.*, *10*, 363–371.

Kamide, Y., and A. Chian (Eds.) (2007), *Handbook of the Solar-Terrestrial Environment*, Springer, New York.

Kozyra, J., M. C. Fok, E. R. Sanchez, D. S. Evans, D. Hamilton, and A. F. Nagy (1998), The role of precipitation losses in producing the rapid early recovery phase of the great magnetic storm of February 1986, *J. Geophys. Res.*, *103*(A4), 6801–6814, doi:10.1029/97JA03330.

Kozyra, J. U., et al. (2002), Multistep *Dst* development and ring current composition changes during the 4–6 June 1991 magnetic storm, *J. Geophys. Res.*, *107*(A8), 1224, doi:10.1029/2001JA000023.

Liemohn, M. W., J. U. Kozyra, C. R. Clauer, and A. J. Ridley (2001), Computational analysis of the near-Earth magnetospheric current system during two-phase decay storms, *J. Geophys. Res.*, *106*, 29,531–29,542.

Lyatsky, W., S. Lyatskaya, and A. Tan (2007), A coupling function for solar wind effect on geomagnetic activity, *Geophys. Res. Lett.*, *34*, L02107, doi:10.1029/2006GL027666.

Maltsev, Y. P., and A. A. Ostapenko (2002), Comment on "Evaluation of the tail current contribution to *Dst*" by N. E. Turner et al., *J. Geophys. Res.*, *107*(A1), 1010, doi:10.1029/2001JA900098.

Maltsev, Y. P., A. A. Arykov, E. G. Belova, B. B. Gvozdevskay, and V. V. Safargaleev (1996), Magnetic flux redistribution in the storm time magnetosphere, *J. Geophys. Res.*, *101*(A4), 7697–7704.

Newell, P., T. Sorelis, K. Liou, C.-I. Meng, and F. Rich (2007), A nearly universal solar wind-magnetosphere coupling function inferred from 10 magnetospheric state variables, *J. Geophys. Res.*, *112*, A01206, doi:10.1029/2006JA012015.

Ober, D. M., N. C. Maynard, and W. J. Burke (2003), Testing the Hill model of transpolar potential saturation, *J. Geophys. Res.*, *108*(A12), 1467, doi:10.1029/2003JA010154.

O'Brien, T. P., and R. L. McPherron (2000), An empirical phase space analysis of ring current dynamics: Solar wind control of injection and decay, *J. Geophys. Res.*, *105*(A4), 7707–7719.

Patra, S., E. Spencer, W. Horton, and J. Sojka (2011), Study of *Dst*/ring current recovery times using the WINDMI model, *J. Geophys. Res.*, *116*, A02212, doi:10.1029/2010JA015824.

Reiff, P. H., and J. G. Luhmann (1986), Solar wind control of the polar-cap voltage, in *Solar Wind-Magnetosphere Coupling*, edited by Y. Kamide and J. A. Slavin, pp. 453–476, Terra Sci., Tokyo.

Sckopke, N. (1966), A general relation between the energy of trapped particles and the disturbance field near the Earth, *J. Geophys. Res.*, *71*(13), 3125–3130.

Siscoe, G. L., G. M. Erickson, B. U. O. Sonnerup, N. C. Maynard, J. A. Schoendorf, K. D. Siebert, D. R. Weimer, W. W. White, and G. R. Wilson (2002a), Hill model of transpolar potential saturation: Comparisons with MHD simulations, *J. Geophys. Res.*, *107*(A6), 1075, doi:10.1029/2001JA000109.

Siscoe, G. L., N. U. Crooker, and K. D. Siebert (2002b), Transpolar potential saturation: Roles of region-1 current system and solar wind ram pressure, *J. Geophys. Res.*, *107*(A10), 1321, doi:10.1029/2001JA009176.

Spencer, E., W. Horton, L. Mays, I. Doxas, and J. Kozyra (2007), Analysis of the 3–7 October 2000 and 15–24 April 2002 geomagnetic storms with an optimized nonlinear dynamical model, *J. Geophys. Res.*, *112*, A04S90, doi:10.1029/2006JA012019.

Spencer, E., A. Rao, W. Horton, and M. L. Mays (2009), Evaluation of solar wind–magnetosphere coupling functions during geomagnetic storms with the WINDMI model, *J. Geophys. Res.*, *114*, A02206, doi:10.1029/2008JA013530.

Takahashi, S., T. Iyemori, and M. Takeda (1990), A simulation of the storm time ring current, *Planet. Space Sci.*, *38*(9), 1133–1141.

Tsyganenko, N. A., and M. I. Sitnov (2005), Modeling the dynamics of the inner magnetosphere during strong geomagnetic storms, *J. Geophys. Res.*, *110*, A03208, doi:10.1029/2004JA010798.

Turner, N. E., D. N. Baker, T. I. Pulkkinen, and R. L. McPherron (2000), Evaluation of the tail current contribution to *Dst*, *J. Geophys. Res.*, *105*(A3), 5431–5439.

Wolf, R., R. Spiro, S. Sazykin, and F. Toffoletto (2007), How the Earth's inner magnetosphere works: An evolving picture, *J. Atmos. Sol. Terr. Phys.*, *69*, 288–302, doi:10.1016/j.jastp.2006.07.026.

W. Horton, Space and Geophysics Laboratory, University of Texas at Austin, Austin, TX 78712-1081, USA.

P. Kasturi, S. Patra, and E. Spencer, Center for Space Engineering, Utah State University, Logan, UT 84322, USA. (espencer@engineering.usu.edu)

M. L. Mays, NASA Goddard Space Flight Center, Greenbelt, MD 20770, USA.